

## REPORT DOCUMENTATION PAGE

Form Approved OMB NO. 0704-0188

The public reporting burden for this collection of information is estimated to average 1 hour per response, including the time for reviewing instructions, searching existing data sources, gathering and maintaining the data needed, and completing and reviewing the collection of information. Send comments regarding this burden estimate or any other aspect of this collection of information, including suggestions for reducing this burden, to Washington Headquarters Services, Directorate for Information Operations and Reports, 1215 Jefferson Davis Highway, Suite 1204, Arlington VA, 22202-4302. Respondents should be aware that notwithstanding any other provision of law, no person shall be subject to any penalty for failing to comply with a collection of information if it does not display a currently valid OMB control number.  
PLEASE DO NOT RETURN YOUR FORM TO THE ABOVE ADDRESS.

1. REPORT DATE (DD-MM-YYYY) 31-12-2013	2. REPORT TYPE Final Report	3. DATES COVERED (From - To) 25-Jul-2009 - 24-Jul-2013		
4. TITLE AND SUBTITLE FINAL REPORT: Dynamics of Radiation and Atoms in Ultrahigh Intensity Laser Fields		5a. CONTRACT NUMBER W911NF-09-1-0390		
		5b. GRANT NUMBER		
		5c. PROGRAM ELEMENT NUMBER 611102		
6. AUTHORS Barry C. Walker		5d. PROJECT NUMBER		
		5e. TASK NUMBER		
		5f. WORK UNIT NUMBER		
7. PERFORMING ORGANIZATION NAMES AND ADDRESSES University of Delaware 210 Hullihen Hall  Newark, DE		8. PERFORMING ORGANIZATION REPORT NUMBER		
9. SPONSORING/MONITORING AGENCY NAME(S) AND ADDRESS (ES) U.S. Army Research Office P.O. Box 12211 Research Triangle Park, NC 27709-2211		10. SPONSOR/MONITOR'S ACRONYM(S) ARO		
		11. SPONSOR/MONITOR'S REPORT NUMBER(S) 54404-PH.10		
12. DISTRIBUTION AVAILABILITY STATEMENT Approved for Public Release; Distribution Unlimited				
13. SUPPLEMENTARY NOTES The views, opinions and/or findings contained in this report are those of the author(s) and should not be construed as an official Department of the Army position, policy or decision, unless so designated by other documentation.				
14. ABSTRACT This grant resulted in quantifying experimentally and theoretically photoionization from the interaction of an ultrastrong field ( $10^{19}$ W/cm $^2$ ) with atoms and small hydrocarbon molecules. The ionization charge states reached by the ionization ranged from 2+ to 26+ with photoelectron energies measured to exceed 1 MeV. The angular distribution of the final electron states were measured to be consistent with sequential ionization of the ions during the pulse. Correlated ionization processes would therefore have to follow closely sequential ionization, i.e. sequential and nonsequential events are estimated to occur within 5 fs of each other during the laser pulse.				
15. SUBJECT TERMS laser, photoionization, strong field, atomic and molecular, optical physics				
16. SECURITY CLASSIFICATION OF: a. REPORT UU		17. LIMITATION OF ABSTRACT UU	15. NUMBER OF PAGES	19a. NAME OF RESPONSIBLE PERSON Barry Walker
b. ABSTRACT UU				19b. TELEPHONE NUMBER 302-740-0257
c. THIS PAGE UU				

## Report Title

### FINAL REPORT: Dynamics of Radiation and Atoms in Ultrahigh Intensity Laser Fields

#### ABSTRACT

This grant resulted in quantifying experimentally and theoretically photoionization from the interaction of an ultrastrong field ( $10^{19}$  W/cm $^2$ ) with atoms and small hydrocarbon molecules. The ionization charge states reached by the ionization ranged from 2+ to 26+ with photoelectron energies measured to exceed 1 MeV. The angular distribution of the final electron states were measured to be consistent with sequential ionization of the ions during the pulse. Correlated ionization processes would therefore have to follow closely sequential ionization, i.e. sequential and nonsequential events are estimated to occur within 5 fs of each other during the laser pulse.

**Enter List of papers submitted or published that acknowledge ARO support from the start of the project to the date of this printing. List the papers, including journal references, in the following categories:**

**(a) Papers published in peer-reviewed journals (N/A for none)**

Received      Paper

08/27/2012 7.00 P. D. Grugan, S. Luo, M. Videtto, C. Mancuso, B. C. Walker. Classical study of ultrastrong nonperturbative-field interactions with a one-electron atom: Validity of the dipole approximation for the bound-state interaction,  
Physical Review A, (05 2012): 0. doi: 10.1103/PhysRevA.85.053407

10/06/2011 3.00 N Ekanayake, B L Wen, L E Howard, S J Wells, M Videtto, C Mancuso, T Stanev, Z Condon, S LeMar, A D Camilo, R Toth, M F Decamp, B C Walker. Dependence of carbon fragments from methane in strong and ultrastrong elliptically polarized laser fields,  
Journal of Physics B: Atomic, Molecular and Optical Physics, (02 2011): 0. doi: 10.1088/0953-4075/44/4/045604

10/06/2011 4.00 Rob Mitchell, N. Ekanayake, A. Watts, S. White, Rob Sauer, L. Howard, M. Videtto, C. Mancuso, S. Wells, T. Stanev, B. Wen, M. Decamp, B. Walker, Sasi Palaniyappan. Ionization of ethane, butane, and octane in strong laser fields,  
Physical Review A, (10 2010): 0. doi: 10.1103/PhysRevA.82.043433

12/19/2013 8.00 Z. Chen, Z. Bond, A. Loether, L. E. Howard, Y. Gao, S. LeMar, S. White, A. Watts, B. C. Walker, M. F. DeCamp. Reconstructing longitudinal strain pulses using time-resolved x-ray diffraction,  
Physical Review B, (07 2013): 0. doi: 10.1103/PhysRevB.88.014302

12/19/2013 9.00 N. Ekanayake, S. Luo, P. D. Grugan, W. B. Crosby, A. D. Camilo, C. V. McCowan, R. Scalzi, A. Tramontozzi, L. E. Howard, S. J. Wells, C. Mancuso, T. Stanev, M. F. Decamp, B. C. Walker. Electron Shell Ionization of Atoms with Classical, Relativistic Scattering,  
Physical Review Letters, (05 2013): 0. doi: 10.1103/PhysRevLett.110.203003

**TOTAL:**      **5**

**Number of Papers published in peer-reviewed journals:**

---

**(b) Papers published in non-peer-reviewed journals (N/A for none)**

Received      Paper

**TOTAL:**

**Number of Papers published in non peer-reviewed journals:**

---

**(c) Presentations**

"Ultrahigh-Efficiency High Harmonic Generation Driven by UV Lasers", 2013 CLEO: QELS\_Fundamental Science, Optical Society of America

"Reconstructing ultrafast acoustic pulses using time-resolved x-ray diffraction", 2013 CLEO: QELS\_Fundamental Science, Optical Society of America

"Substitution effects in strong and ultrastrong field photoionization of chloromethane and dichloromethane", Bulletin of the American Physical Society 58, 2013 DAMOP, American Physical Society

**Number of Presentations:** 3.00

**Non Peer-Reviewed Conference Proceeding publications (other than abstracts):**

Received      Paper

**TOTAL:**

**Number of Non Peer-Reviewed Conference Proceeding publications (other than abstracts):**

---

**Peer-Reviewed Conference Proceeding publications (other than abstracts):**

Received      Paper

**TOTAL:**

**Number of Peer-Reviewed Conference Proceeding publications (other than abstracts):**

---

**(d) Manuscripts**

Received      Paper

03/30/2010 2.00 Sasi Palaniyappan, Rob Mitchell, N. Ekanayake, A.M. Watts, S.L. White, Rob Sauer, L.E. Howard, M. Videtto, C. Mancuso, S.J. Wells, T. Stanev, B.L. Wen, M.F. Decamp, and B.C. Walker. Ionization of Ethane, Butane, and Octane in Strong Laser Fields, Physical Review A (03 2010)

08/27/2012 6.00 N. Ekanayake, Sui Luo, B.L. Wen, L.E. Howard, S.J. Wells, M. Videtto, C. Mancuso, T. Stanev, Z. Condon, S. LeMar, A. Camilo, R. Toth, W. Crosby, P. Grugan, M. Decamp, B. Walker. Rescattering Nonsequential Ionization of Ne $^{3+}$ , Ne $^{4+}$ , Ne $^{5+}$ , Kr $^{5+}$ , Kr $^{6+}$ , Kr $^{7+}$ , and Kr $^{8+}$  in a Strong, Ultraviolet, Ultrafast Laser Field, Physical Review A (08 2012)

10/06/2011 5.00 Pat Grugan, Sui Luo, Mike Videtto, Chris Mancuso, Barry Walker. Classical Ionization of Atoms by an Ultrastrong Field, (10 2011)

**TOTAL:**      **3**

**Number of Manuscripts:**

**Books**

Received      Paper

**TOTAL:**

**Patents Submitted**

**Patents Awarded**

**Awards**

Elected as Fellow of the American Physical Society

### Graduate Students

<u>NAME</u>	<u>PERCENT_SUPPORTED</u>	Discipline
Nagitha Ekanayake	0.50	
Patrick Grugan	0.50	
<b>FTE Equivalent:</b>	<b>1.00</b>	
<b>Total Number:</b>	<b>2</b>	

### Names of Post Doctorates

<u>NAME</u>	<u>PERCENT_SUPPORTED</u>
<b>FTE Equivalent:</b>	
<b>Total Number:</b>	

### Names of Faculty Supported

<u>NAME</u>	<u>PERCENT_SUPPORTED</u>	National Academy Member
Barry Walker	0.10	
<b>FTE Equivalent:</b>	<b>0.10</b>	
<b>Total Number:</b>	<b>1</b>	

### Names of Under Graduate students supported

<u>NAME</u>	<u>PERCENT_SUPPORTED</u>	Discipline
Alex Daniels	0.25	
Tim Halter	0.25	
<b>FTE Equivalent:</b>	<b>0.50</b>	
<b>Total Number:</b>	<b>2</b>	

### Student Metrics

This section only applies to graduating undergraduates supported by this agreement in this reporting period

The number of undergraduates funded by this agreement who graduated during this period: ..... 2.00

The number of undergraduates funded by this agreement who graduated during this period with a degree in science, mathematics, engineering, or technology fields:..... 2.00

The number of undergraduates funded by your agreement who graduated during this period and will continue to pursue a graduate or Ph.D. degree in science, mathematics, engineering, or technology fields:..... 1.00

Number of graduating undergraduates who achieved a 3.5 GPA to 4.0 (4.0 max scale):..... 2.00

Number of graduating undergraduates funded by a DoD funded Center of Excellence grant for Education, Research and Engineering:..... 0.00

The number of undergraduates funded by your agreement who graduated during this period and intend to work for the Department of Defense ..... 0.00

The number of undergraduates funded by your agreement who graduated during this period and will receive scholarships or fellowships for further studies in science, mathematics, engineering or technology fields: ..... 0.00

### Names of Personnel receiving masters degrees

NAME

**Total Number:**

**Names of personnel receiving PhDs**

NAME

Nagitha Ekanayake

**Total Number:**

1

**Names of other research staff**

NAME

PERCENT SUPPORTED

**FTE Equivalent:**

**Total Number:**

**Sub Contractors (DD882)**

**Inventions (DD882)**

**Scientific Progress**

**Technology Transfer**

## FOREWARD

This report is broken into the main research findings. It is a summary of all work done under the grant. Detailed descriptions are available in the published manuscripts. The grant was invaluable in its support of the terawatt laser facility, graduate students, and undergraduate students:

PhD: Nagitha Ekanayake, Patrick Grugan, Laura Barclay, Zachary Bond, Sui Luo

BS and BA: Arielle D. Camilo, Ivette Planell-Mendez, Sara LeMar, Zach Condon, Lauren Howard, Willow Crosby, Anthony Tramontozzi, Caitlin V. McCowan, Rosie Scalzi, Sarah Wells, Alejandro Londono, Sarah Wells, Teddy Stanev, Tim Halter, Alex Daniels.

The results stand as some of the only studies on ultrastrong field interactions with atoms and molecules.

## STATEMENT OF THE PROBLEM STUDIED

The research goal was to understand the basic physics of the interaction of an ultrastrong laser fields with atoms, ions, and small to medium size molecules. The range of laser intensities used began at  $10^{14}$  W/cm<sup>2</sup> and extended beyond  $10^{19}$  W/cm<sup>2</sup>. Important questions addressed include (1) the role of the magnetic field from the laser and (2) collective effects in the atoms, ions, and molecules. Significant progress was made on both topics. The studies were both theoretical and experimental in nature. The next generation of problems will follow on these studies and address how much of the atom and the electrons it is possible to excite with the 1,000 eV to 1,000,000 eV electron energies typical of these interactions as well as how these excitations occur and can be controlled in atoms and molecules.

## CONTENTS AND RESULTS

- 1) Role of the Laser Magnetic Field in Ultra-Intense Fields: Semi-Classical Calculations Of Ionization (Theory)
- 2) Dependence of Carbon Fragments From Methane in Strong And Ultrastrong Elliptically Polarized Laser Fields (Experiment and Theory)
- 3) Ultrastrong, Nonperturbative Field Interactions with a One-electron Atom: Validity of the Dipole Approximation for the Bound State Interaction (Theory)
- 4) Ionization of Neon and Krypton in a Strong, Ultraviolet, Ultrafast Laser Field (Experiment and Theory)
- 5) Photoelectrons from Ultra-Strong Fields (Experiment and Theory)
- 6) Reconstructing Longitudinal Strain Pulses Using Time-Resolved X-Ray Diffraction (Experiment and Theory)

## ROLE OF THE LASER MAGNETIC FIELD IN ULTRA-INTENSE FIELDS: SEMI-CLASSICAL CALCULATIONS OF IONIZATION

We present a classical Monte Carlo simulation where we numerically integrate the classical equations of motion for single electron atoms interacting with an external laser pulse. Atoms with atomic numbers  $1 < Z < 15$  are studied to determine the influence of the laser magnetic field on the ionization process. We find the dipole approximation ( $B=0$ ) is valid up to intensities of  $10^{22} \text{ W/cm}^2$  for calculating the ionization rate. A small Lorentz deflection is seen in the angular distribution of ionized electrons as the intensity is increased well into the relativistic regime as the magnetic field begins to deflect the electron as tunnel ionizes.

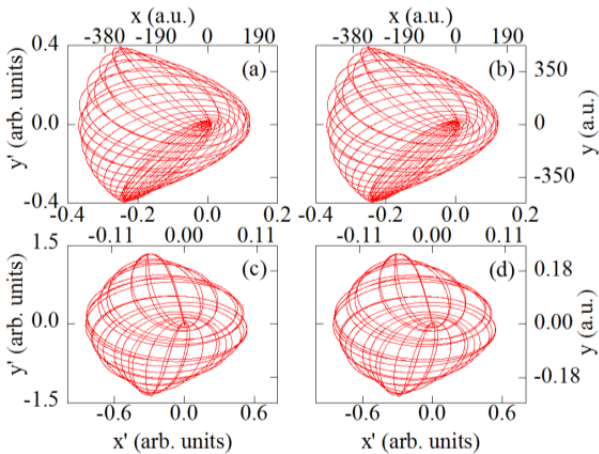


FIG. 1: Procession of the orbits. The  $x'$  effective coordinates have been rescaled by the square root of the electric field strength. Classical, nonrelativistic Rydberg trajectories are shown in (a) & (b) are for  $Z = 1$ , Rydberg state ( $n,l = 18,s$ ) with and without magnetic field respectively. The

trajectories for (c) & (d) are for tightly bound ( $n,l = 1,s$ ) state for  $Z = 8$ , with and without magnetic field, respectively (a.u. is for atomic units).

The figure shows that despite the increase in the field magnitude by more than  $10^9$  the trajectories are similarly unaffected by the inclusion of the laser magnetic field. While this is expected for the 18s Rydberg state ionized by microwave radiation, this result was not anticipated at such high intensities ( $> 10^3$  a.u.) and tightly bound states ( $z=8$ ) considered well into the relativistic regime for the laser-matter interaction. We quantified the differences with and without the laser magnetic field by looking at the phase space, configuration space explored by the electron with and without the laser magnetic field, comparing the ionization rates, and finally looking at the momentum in the angular distributions of the outgoing electrons.

The difference in the configuration space visited by the electron during the interaction with the laser field is shown in Fig. 2. For these distributions we mark out a spatial grid ranging from  $-4n^2/Z < x, y, z < 4n^2/Z$ . The coordinates of the electron are averaged over time for  $10^4$  electrons. We subtract the distributions calculated with the laser electric and magnetic field (denoted E&B) from the calculated distribution calculated including only the laser electric field (denoted E). To set the numerical accuracy estimate we calculate the configuration space for two different random number launches of the  $10^4$  electrons and subtract the two calculations, i.e.  $(E\&B)_1 - (E\&B)_2$ .

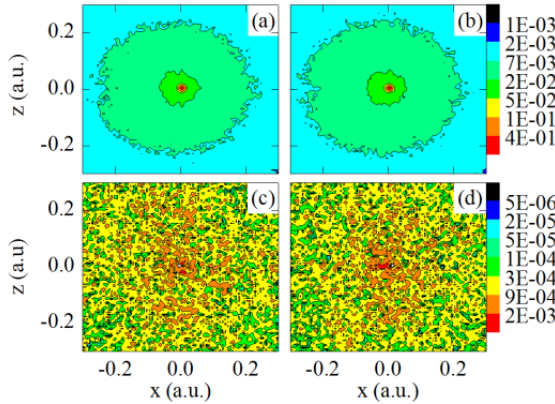


FIG. 2: Configuration space distributions for  $Z = 4$ . (a) Distribution in the dipole approximation. (b) Distribution with magnetic field included. (c) Difference in normalized distributions  $\text{Sqrt}[(E-E\&B)^2]$ . (d) Difference in two sets of distributions  $\text{Sqrt}[(E\&B)_1-(E\&B)_2^2]$ .

We find no differences in configuration space when including  $(E\&B)$  and neglecting  $(E)$  the laser magnetic field. Any differences we note are at the level of  $10^{-4}$ , which is similar to the noise from the numerical calculations and different random number launches. Therefore, there is no appreciable difference in the configuration space distributions. Surprisingly, this result shows the ultrastrong external field of order  $10^3$  a.u. is actually very weak compared to the relevant bound state interactions and result in no significant perturbation of the electron. This is consistent with the ionization critical field seen in Fig. 3 where we see no significant difference in the critical field required to achieve ionization at the intensity changes from 0.001 a.u. to  $10^6$  a.u. of intensity.

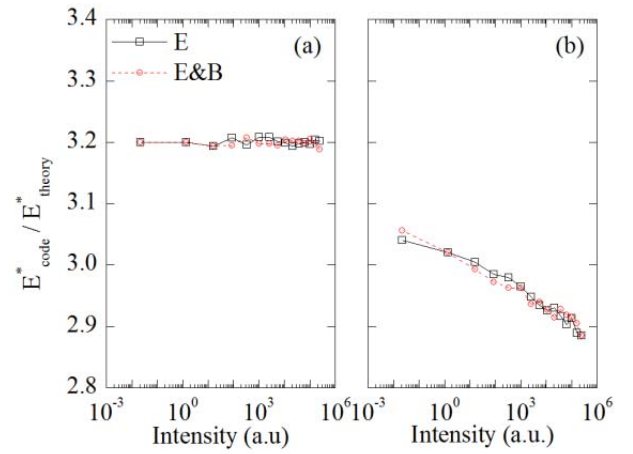


FIG. 3: Ratio of critical field from numerical integration to theoretical value (a) 3D conditions and (b) x-z 2D plane conditions.

Finally we show the angular distributions calculated using the coordinates of the electron as it ionizes. With the inclusion of the magnetic field, the magnetic field can cause the electron trajectory to deflect via the Lorentz force. The change in the range of angles can give an indication of the amount of deflection the electron experiences. For  $Z < 3$  the relative difference in the range of angles is almost negligible for all intensities considered. When  $Z > 3$  the range of angles increases. Figure 4 shows the angular distributions for three different  $Z$  values for both the dipole approximation and non-dipole approximation. The intensity for these species is:  $Z=1$  the intensity to ionize is 0.01 a.u.,  $Z=5$  the intensity to ionize is 300 a.u., and  $Z=10$  the intensity to ionize is  $2 \cdot 10^4$  a.u.

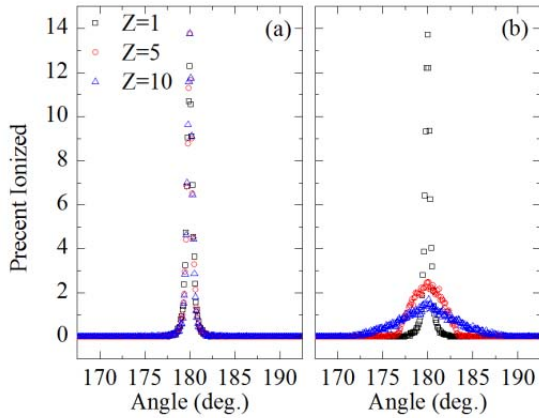


FIG. 4: Angle of emission for the ionized electron from  $Z=1$  to  $Z=10$  species without the laser magnetic field (a) and with the laser magnetic field (b).

In conclusion, we investigated the influence of including the laser magnetic field on the ionization process. We have seen that the dipole approximation is still valid for intensities up to  $10^{22} \text{ W/cm}^2$  and the laser magnetic field has little to no influence on bound state dynamics for the electron. We have also seen that angular distributions of ionized electrons will be slightly affected by inclusion of the laser magnetic field at ultrahigh intensities when the ionized electron is tightly bound.

# DEPENDENCE OF CARBON FRAGMENTS FROM METHANE IN STRONG AND ULTRASTRONG ELLIPTICALLY POLARIZED LASER FIELDS

We present the ellipticity dependence of the ultrafast photoionization for  $C^{n+}$  fragments from methane. The study extends from the strong field ( $C^+$ ,  $C^{2+}$ ) at  $10^{14}$  W/cm<sup>2</sup> to the ultrastrong field ( $C^{5+}$ ) at  $10^{18}$  W/cm<sup>2</sup>. The measurements show  $C^+$  and  $C^{2+}$  ionization have limited sensitivity to the field polarization. As the laser intensity and corresponding degree of ionization increase ( $C^{4+}$ ,  $C^{5+}$ ), the dependence on the field polarization increases. Comparisons to a semi-classical field ionization model shows the ellipticity dependence of the relative ion

When the returning electron inelastically rescatters with the parent ion, it may remove one or more additional electrons leading to

yield for higher charge states comes from the field dependence of tunneling ionization rather than nonsequential ionization due to rescattering. A movement from a molecule-like response to an atom-like response with the increase in intensity is observed. Figure 1 demonstrates the role of ellipticity on the photoelectron ionized at  $x,y = 0,0$  with a semiclassical trajectory ensemble of ionization. For linear polarization (a) the electron moves in 1D along the x axis while it spreads in the continuum. As the laser field polarization goes from linear to elliptical (b) to circular polarization (c) the photoelectron is driven more and more in 2D along the y-axis. As a result, the photoelectron with circularly polarized light (c) never returns to the origin (0,0) to revisit the ion core.

multi-electron nonsequential ionization (NSI), excite inner shell electrons, or release the energy as high harmonic generation

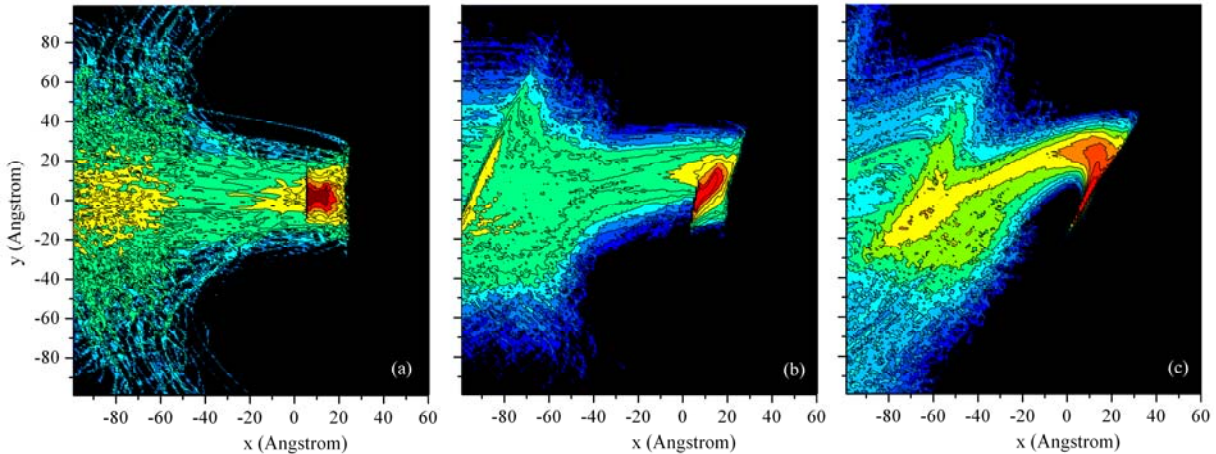


Fig. 1: Density plot for 5000 calculated photoelectron trajectories from  $C^+$  located at the origin (0,0) as a function of time. The initial ionization considered in the figure begins 0.35 radians after the peak of the 800 nm laser field ( $\hat{E} = -\hat{x}$  at this phase). The field is linearly polarized ( $\epsilon = 0$ ) in (a), elliptically polarized ( $\epsilon = 0.5$ ) in (b), and circularly polarized ( $\epsilon = 1$ ) in (c). The trajectories are plotted for a little less than one optical cycle.

(HHG). Using elliptically polarized light the returning electron can be adjusted to control NSI and HHG. In molecular systems, the rescattering electron wave has been used to provide precision measurements of the molecular electron wave function and orbital tomography. Rescattering driven by elliptically polarized light has also been used to image dynamics within molecular orbits by causing the rescattering electron motion to interact with different spatial portions of the molecular ion wave function. Here we present the results of our investigation into the dependence of the  $C^{n+}$  fragmental ions on ellipticity. New data on the polarization dependence of the ultrastrong field interaction is presented to provide important information about electron dynamics and the ionization of methane in strong and ultrastrong laser fields.

Figure 2 shows the intensity dependent yield of the atomic fragmental ions  $C^{n+}$  ( $1 \leq n \leq 5$ ) from methane between  $4 \times 10^{13}$  to  $1 \times 10^{19}$   $W/cm^2$ . Also shown in the figure are the calculated tunneling ionization yields for  $C^{n+}$ , expected from ionizing atomic carbon with the experimental laser parameters. The ionization yields for  $C^+$  and  $C^{2+}$  increase smoothly (with an  $I^5$  dependence for example with  $C^{2+}$ ) from the detection threshold of 0.1 ion / shot-torr to saturation at  $10^5$  ions / shot-torr in the intensity range near  $10^{14} W/cm^2$ . Above  $10^5$  ions / shot-torr the yield is saturated and the intensity dependence is  $I^{3/2}$  as expected for collections from a Gaussian laser focus. The observed intensity dependence for  $C^+$  and  $C^{2+}$  is close to that observed for the molecular fragments in Fig. 2 with an appearance near  $5 \times 10^{13} W/cm^2$  and saturation near  $3 \times 10^{14} W/cm^2$ .

The yields of  $C^{4+}$  and  $C^{5+}$  are more complicated. Most apparent is the presence of a characteristic “knee” structure in the intensity dependent ion yield at a few percent of the saturated yield, i.e.  $10^2$  to  $10^3$  ions / shot-torr. This clear signature of NSI begins at  $10^{15} W/cm^2$  for  $C^{4+}$  and is also prominent beginning at  $10^{16} W/cm^2$  in  $C^{5+}$ .

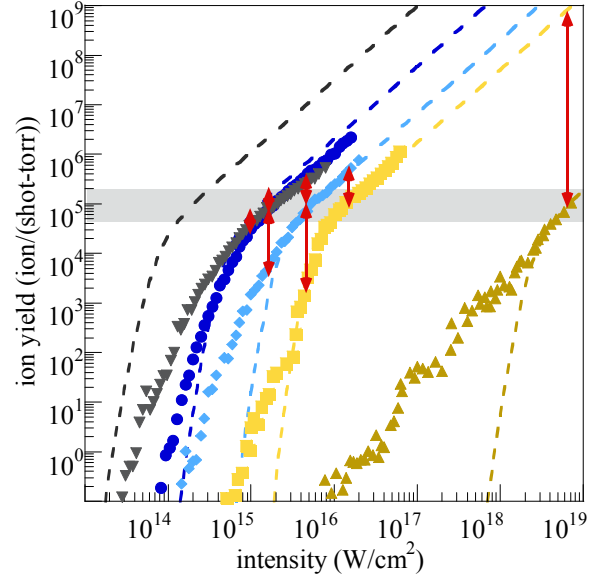


Fig. 2:  $C^{+1}$  (gray invert triangle),  $C^{2+}$  (blue circle),  $C^{3+}$  (light blue diamond),  $C^{4+}$  (yellow square) and  $C^{5+}$  (brown triangle) ion yields as a function of linearly polarized laser pulse intensity. The data is plotted with the calculated single electron, linearly polarized tunneling ionization yields (dashed). Red arrows on the ion curves indicate points where the ellipticity dependence was taken. The grayed area near  $10^5$  ions/(shot-torr) indicates the region where the ionization begins to saturate.

The ellipticity collections of the ionization yields are presented in Fig. 3 as ratios of adjacent charge states  $C^{(n+1)+}/C^{n+}$  versus the field polarization  $\epsilon$ . The measurements were taken at intensities where one of the charge

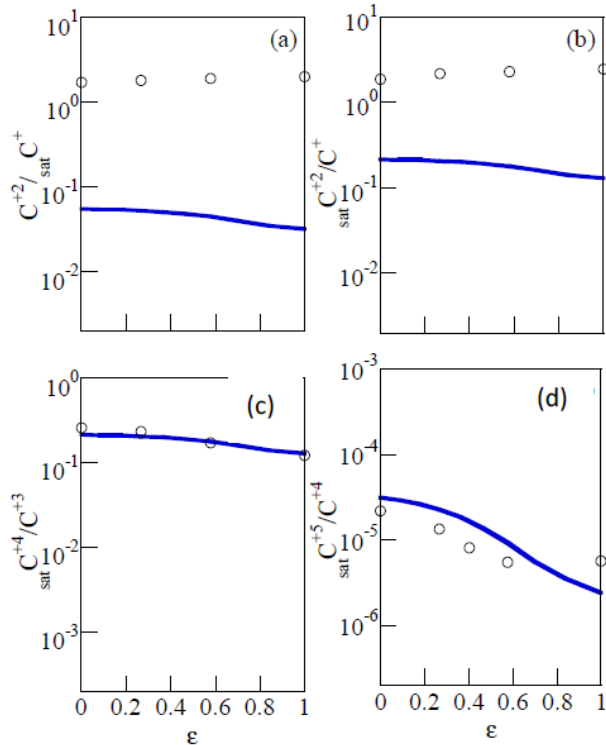


Fig. 3: Ellipticity dependence of  $\text{satC}^{(n+1)+}/\text{C}^{n+}$ ) where the ‘sat’ subscript denotes the species in the collection which is saturated (approximately  $10^5$  ions/(shot-torr) in Fig. 3) at that intensity:  $9 \times 10^{14}$  (a),  $1.5 \times 10^{15}$  (b),  $1.3 \times 10^{16}$  (c), and  $7.0 \times 10^{18}$   $\text{W/cm}^2$  (d) in the collection. The calculated result is also shown in the data (solid line).

states in this ratio is near saturation:  $9 \times 10^{14}$ ,  $1.5 \times 10^{15}$ ,  $4.0 \times 10^{15}$ ,  $1.3 \times 10^{16}$ , and  $7.0 \times 10^{18}$   $\text{W/cm}^2$  for  $\text{C}^+$ ,  $\text{C}^{2+}$ ,  $\text{C}^{3+}$ ,  $\text{C}^{4+}$ , and  $\text{C}^{5+}$ , respectively.

These ellipticity collection points are superimposed on the ion yields in Fig. 3. What is immediately clear in the collections is the relative similarity in the yields of  $\text{C}^+$  and  $\text{C}^{2+}$ . When expressed as a ratio the result is unity magnitude with no real dependence on polarization over the full range of polarizations  $0 < \epsilon < 1$ . Moving to higher intensities and charge states, the ratios become more dependent on the laser

polarization. The half width at half maximum (hwhm) for  $\text{C}^{4+}/\text{satC}^{3+}$  is  $\Delta\epsilon_{\text{hwhm}} = 0.4$  and for  $\text{C}^{5+}/\text{satC}^{4+}$  is  $\Delta\epsilon_{\text{hwhm}} = 0.32$ . Comparisons to the atomic model (Fig. 3 solid line) also show excellent agreement with the experiments for high intensities and charge states while for lower charge states the agreement is poor.

We present measurements and calculations on the field polarization dependence for the carbon fragments from the strong and ultrastrong field ionization of methane. These studies show the formation of lower charge states, i.e.  $\text{C}^+$  and  $\text{C}^{2+}$ , have little dependence on the field polarization and are in poor agreement with an atomic like model of ionization, consistent with the strong role of molecular mechanisms at lower intensity interactions. However, the higher charge states,  $\text{C}^{4+}$  and  $\text{C}^{5+}$ , do exhibit dependence on the field polarization and are in agreement with a semi-classical tunneling rescattering model. The interpretation from the model and data comparison indicates as the intensity is increased the ionization in methane evolves from a molecular response for the valence electrons involved in bonding to an atomic mechanism for the inner shell  $1s^2$  electrons.

## ULTRASTRONG, NONPERTURBATIVE FIELD INTERACTIONS WITH A ONE-ELECTRON ATOM: VALIDITY OF THE DIPOLE APPROXIMATION FOR THE BOUND STATE INTERACTION

Ionization is an essential response of the atom to a strong external field. It is an interaction that spans from Rydberg atoms in microwave radiation to multielectron excitation in strong and ultrastrong optical frequency fields. Advances in laser technology continue to push the boundaries of this interaction in frequency and intensity with the emergence of 4th generation free electron lasers, high peak power terawatt and petawatt lasers. Many strong field models that address the interaction of these sources with atoms and molecules capitalize on the dipole approximation, where the laser magnetic field is assumed to be zero ( $B_{\text{laser}}=0$ ) and the physics is dominated by the external electric field ( $E_{\text{laser}}$ ). As the external field and velocity of the interacting atomic or molecular states increase, this approximation will breakdown.

The new frontier in ultrastrong radiation-matter interactions has attracted significant theoretical interest. Yet precision experimental results up to intensities as high as  $10^{19} \text{ W/cm}^2$  have not observed any affect of  $B_{\text{laser}}$  on the one-electron ionization yield. Recent experiments and models have included  $B_{\text{laser}}$  in their treatment of phenomena and address primarily photoelectron final states and rescattering. Photoelectron final state measurements verified the forward deflection of the photoelectron in the continuum due to the large momentum transfer from the photons to the electron and also revealed the angular distributions of these photoelectrons. Ultrastrong field rescattering models address the continuum electron and its deflection by the  $B_{\text{laser}}$  Lorentz force as it is being accelerated by  $E_{\text{laser}}$ . In the rescattering process,  $B_{\text{laser}}$  is believed to have an influence above intensities of  $3 \cdot 10^{16} \text{ W/cm}^2$  for optical fields and more generally when the relativistic rescattering parameter  $\gamma_R > 1$  where  $\gamma_R = (U_p^3 V_{\text{IP}})^{1/2} / (3 c^2 \omega)$  for a radiation field with a peak magnitude of  $E_0$ , speed of light  $c$ , carrier frequency of  $\omega$ , ponderomotive energy of  $U_p = E_0^2 / 4\omega^2$ , and  $V_{\text{IP}}$  ionization potential.

Rescattering and photoelectron final state research deal with the result of the ultrastrong external magnetic field interaction after the electron ionizes. There are still fundamental questions on how the ultrastrong field affects the bound state dynamics and 'birth' of the photoelectron. It has been reported that even in the intensity range of  $10^{17} \text{ W/cm}^2$  to  $10^{18} \text{ W/cm}^2$  for quasistatic as well as high frequency, stabilization fields, the magnetic field can influence ionization. A clear understanding of the ionization mechanism is a crucial insight into the physics behind the ultrastrong field interaction. Conceivably, it is possible ultrastrong magnetic fields and the electron cyclotron frequency in the bound state can create dynamics, such as is the case for 'cycloatoms'. Because the strong field is comparable to the Coulomb field, these interactions are beyond the traditional, perturbative response.

A detailed classical study on the effects of  $B_{\text{laser}}$  in the ionization process was undertaken with the objective to determine the validity of the dipole approximation for the bound state interaction in a regime well known to be relativistic and require a full  $E_{\text{laser}}$  and  $B_{\text{laser}}$  treatment for the continuum. This study addresses when the magnetic field begins to affect the bound state and to what extent in the ultrastrong field interaction a dipole interaction can be used to calculate the ionization probability. By studying classical electron dynamics, a physical model of strong field ionization has been gained for a number of phenomena including harmonic generation and complex multielectron phenomena. Furthermore, as the fields and energy of the electron increase, there is an indication strong external field interactions will become more classical. We present here calculations describing the influence of  $B_{\text{laser}}$  on the bound state and ionization for an atom at 'relativistic', ultrastrong intensities. We address bound state dynamics of the electron by inspecting electron ensemble trajectories in configuration space during the interaction. Also, we calculate  $B_{\text{laser}}$  induced changes in the ionization rate as a function of field strength and inspect angular distributions for the photoelectrons when they first appear, or are 'born' in the continuum. In this summary we will only show the configuration results in detail.

In our calculations, the atom is treated as a single electron, hydrogen-like system. This is motivated by the success of the single active electron approximation in strong fields where the 'outer', least-tightly bound electron (typically in the ground state) directly interacts with the external field and the 'inner', core electrons do not. With the  $10^3$  eV to  $10^6$  eV electron energies in ultrastrong fields, multielectron processes are significant but single electron processes remain a primary mechanism. Our second approximation is the classical description of the electron and field, following the dynamics with trajectories. The classical treatment of strong fields is a well established technique and allows the investigation of full three-dimensional dynamics currently intractable with relativistic quantum calculations.

For correspondence to the quantum case, we use bound state energies  $E_n = -Z^2/2n^2$  where  $n$  is the principle quantum number and  $Z$  is the atomic number. The angular momentum of the electron is varied between 0 and  $\hbar$ . The choice of angular momentum in this range does not change the results presented here. Quantum uncertainty and probability is mimicked in our classical system by giving position and momentum distributions to the microcanonical Monte Carlo ensembles consistent with the uncertainty principle. In determining the initial position and momentum of the electrons we follow the method given in. The Kepler orbits are defined by a set of five parameters: inclination of the orbit ( $i$ ); ascending node longitude ( $\Omega$ ); mean anomaly ( $\alpha$ ); orbit eccentricity ( $e$ ); and an argument of pericenter ( $\omega_A$ ). These parameters are generated randomly to create 3D ensembles for the electron and can take on the values,

$$0 \leq \alpha \leq 2\pi, \quad 0 \leq e^2 \leq 1, \quad -1 \leq \cos i \leq 1, \\ 0 \leq \Omega \leq 2\pi, \quad 0 \leq \omega_A \leq 2\pi$$

The values of position and momenta as functions of time are generated by integrating Hamilton's equations of motion for the electron in a soft core potential.

$$\frac{dp_x}{dt} = -\frac{Ze^2 x}{(r^2 + \delta)^{3/2}} - eE_{\text{laser}}(\vec{r}, t) \left[ 1 - \frac{p_z}{\sqrt{p^2 + m_0^2 c^2}} \right], \quad (1)$$

$$\frac{dp_y}{dt} = -\frac{Ze^2 y}{(r^2 + \delta)^{3/2}}, \quad (2)$$

$$\frac{dp_z}{dt} = -\frac{Ze^2 z}{(r^2 + \delta)^{3/2}} - eE_{\text{laser}}(\vec{r}, t) \frac{p_x}{\sqrt{p^2 + m_0^2 c^2}}, \quad (3)$$

$$\frac{dx}{dt} = \frac{p_x c}{\sqrt{p^2 + m_0^2 c^2}}, \quad (4)$$

$$\frac{dy}{dt} = \frac{p_y c}{\sqrt{p^2 + m_0^2 c^2}}, \quad (5)$$

$$\frac{dz}{dt} = \frac{p_z c}{\sqrt{p^2 + m_0^2 c^2}}, \quad (6)$$

Where  $c$  is the speed of light,  $\delta$  is our soft core parameter,  $Z$  is the atomic number,  $e$  is the charge,  $m_0$  is the rest mass,  $r = \sqrt{x^2 + y^2 + z^2}$  and  $p = \sqrt{p_x^2 + p_y^2 + p_z^2}$ . When the dipole approximation is considered, the Lorentz force term from  $B_{\text{laser}}$  is dropped in eq. 1 and in eq. 3. The value of  $\delta$  is chosen to keep the energy of the electron less than 5 MeV at  $r = 0$ . We also verified using a Coulomb potential with an  $r = 0$  exit condition (e.g. excluding results for trajectories that come close enough to  $r = 0$  so their energy would exceed 5 MeV) does not change the outcome. Spin is neglected as it does not affect ionization at the level of 5 % until  $Z = 60$ . The accuracy of the solutions can be gauged by the conservation of energy in the absence of the external radiation field. In this case, the energy deviates by less than  $10^{-9}$  after 200 Kepler orbits for any state used in the calculation.

Our field is a linearly polarized plane wave propagating in  $z$  with  $E_{\text{laser}}$  in the  $x$  direction. We linearly increase the field over many Kepler orbits,  $\tau_K = 2\pi n^3/Z^2$ , of the state being ionized and then hold the field constant at a maximum value. The ramp rate of 50  $\tau_K$  from zero to the maximum is safely in the adiabatic limit, which begins to breakdown in our calculations for ramps faster than 5  $\tau_K$ . After the ramp, the field is held constant at the maximum value for an additional 50  $\tau_K$ . To calculate angular distributions we employ a  $\sin^2$  pulse shape with a full-width-at-half-maximum of 200  $\tau_K$ .

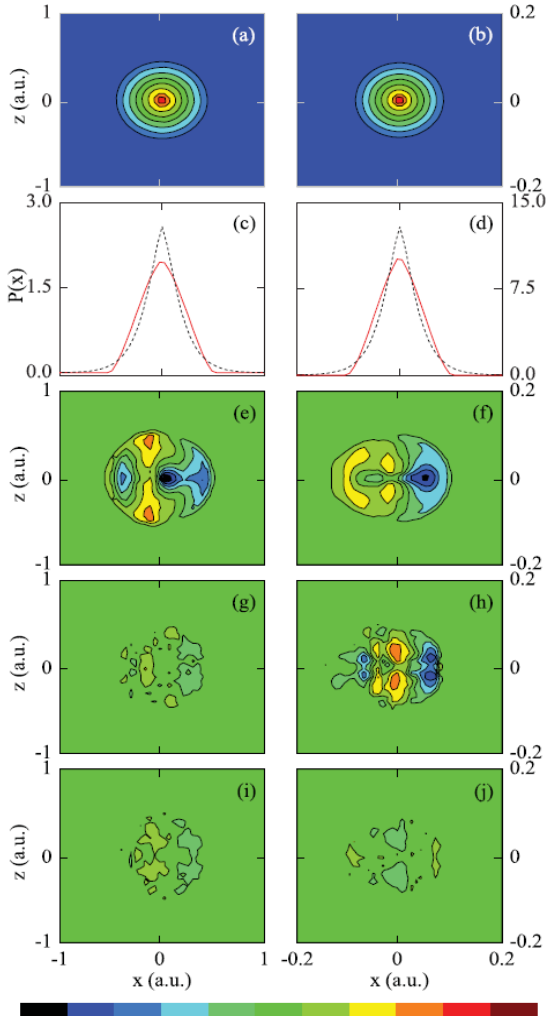


Fig. 1: Configuration space distributions for  $Z=4$  (a,c,e,g,i) and  $Z=20$  (b,d,f,h,j). The configuration space with no external laser field is shown in (a,b). A line out of the classical configuration space compared with the quantum wave function probability,  $P(x)$ , is in (c,d). The differences between the configuration space with no external field and an external  $E_{\text{laser}}$  field with a peak value of 9.8 a.u. for  $Z=4$  and 710 a.u. for  $Z=20$  are shown in (e,f). The difference between the configuration space with the full  $E_{\text{laser}}$ ,  $B_{\text{laser}}$  fields (9.8 a.u. for  $Z=4$ , 710 a.u. for  $Z=20$ ) and the dipole approximation are in (g,h). An estimate of numerical fluctuations within the configuration space plots is shown in (i,j) as determined by subtracting two ensembles that differ only in the trajectory initial conditions for the  $10^5$  trajectories. The color assignment shown at the bottom of the figure ranges from 0 (black) to 1 (red) for (a,b). The range for the other plots is -0.16 (black) to +0.16 (red) for (e,f) and -0.016 (black) to +0.016 (red) for (g,h,i,j).

Similar results are achieved with the ramped field pulse shape. The calculations are done in the quasistatic limit with carrier frequencies from zero to one-twentieth of the Kepler orbit frequency.

To examine full ensembles of  $10^4$  to  $10^5$  trajectories, we turn to probabilities within configuration space. The probability distributions presented are a time average over a 1000 by 1000 spatial grid. For the 2D, x-z plot we integrate over the y coordinate. The  $(Z,n) = (4,1)$  and  $(20,1)$  states for the figure are for the strong field and ultrastrong field interaction, respectively. We have chosen to show these results for a low frequency field which polarizes the atom in one direction. The results in the figure as shown are indistinguishable for fields with a carrier frequency from d.c. to 0.007 a.u. for  $Z=4$  and frequencies from d.c. to 0.18 a.u. for  $Z=20$ . The choice of the low frequency presentation was to allow any dynamics from the field polarization to be clearly seen. Results for frequencies that are still quasistatic but approaching the Kepler frequency are shown in Appendix A for frequencies of 0.07 a.u. ( $Z=4$ ) and 1.8 a.u. ( $Z=20$ ).

To begin we show the bound state configuration spaces with no external field in Fig. 1(a,b). For comparison, the electron probability is compared in Fig. 1(c,d) to the quantum wave function probability calculated using the Schrodinger equation. Next we plot the configuration space with an  $E_{\text{laser}}$  only external field ( $B_{\text{laser}}=0$ ) ramped up to a value where roughly one-third of the trajectories ionize by the end of the interaction in Fig. 1(e,f). For the  $(4,1)$  state this is an external field of 10 a.u. and for the  $(20,1)$  case the ultrastrong field is 710 a.u. The results are shown with the bound state configuration space (Fig. 1(a,b)) subtracted. The probability magnitude range for these differences in Fig. 1(e,f) is 16 % of the range shown for the field free distributions in Fig. 1(a,b).

Polarization, aligned orbitals, and ionization effects are all visible in Fig. 1(e,f). The polarization response is visible by the elongation of the probability along  $E_{\text{laser}}$  and a slight shift of the probability along  $-x$ , i.e. a deficiency for  $x > 0$  and overall increase for  $x < 0$ . Alignment effects are evident by the preservation of certain orbits in

configuration space. The alignment effect corresponds to the the quantum case where  $m$  states aligned along  $E_{\text{laser}}$  have different ionization rates. The highest ionization rates are for  $m=0$  (no magnetic moment along  $E_{\text{laser}}$ ) since the electron passes by the tunneling region in the potential on each orbit. States orbiting with a magnetic moment aligned with or against  $E_{\text{laser}}$  are less likely to ionize and the two lobes from the projection of this orbit in the  $x$ - $z$  plane are most clearly seen at  $x = 0$ ,  $z = \pm 0.4$  a.u. in Fig. 1(e).

Finally we give the configuration space with the full  $E_{\text{laser}}$ ,  $B_{\text{laser}}$  field. To highlight any difference we show this result in Fig. 1(g,h) after subtracting the  $E_{\text{laser}}$  only configuration space used in Fig. 1(e,f). The resulting range in Fig. 1(g,h) is 1.6 % of that shown for the field free distributions in Fig. 1(a,b). The calculated noise floor (Fig. 1(i,j)) is obtained from the subtraction of configuration spaces for full  $E_{\text{laser}}$  and  $B_{\text{laser}}$  external field calculations with two different random number trajectory ensemble launches and the same 1.6 % range as in Fig. 1(g,h).

Figure 1(h) shows including  $B_{\text{laser}}$  alters the most stable trajectory regions in configuration space, i.e. trajectories that are more stable against ionization. These  $B_{\text{laser}}$  induced shifts are not present in the nonrelativistic case Fig. 1(g) but are clearly visible features in Fig. 1(h) that result from the interaction of  $B_{\text{laser}}$  on the bound state. The changes in Fig. 1(h) are at the few percent level in the configuration space for an intensity of  $10^{23}$  W/cm<sup>2</sup>. One may speculate for the quantum case these shifts would be manifested by a change in the distribution of the ionization among the  $m$ -states.

A natural progression is clear. At optical frequencies, the dipole interaction is valid for all length scales up to intensities of 1 a.u., as the intensity increases the continuum dynamics and rescattering begin to be affected by  $B_{\text{laser}}$  for intensities beyond 1 a.u. As the field is further increased, we show in these studies the photoelectron angular distribution are slightly affected for intensities near or exceeding  $10^4$  a.u. Up to intensities of  $10^7$  a.u. we do not find  $B_{\text{laser}}$  significantly affects the ionization rate though some

impact at the level of 1 % can be seen in population distributions of the bound state.

In conclusion, we find the dipole approximation is generally valid with classical ionization for intensities up to  $10^{23}$  W/cm<sup>2</sup>. The laser magnetic field has little influence on bound state dynamics for the electron and slightly shifts the bound state population in the ultrastrong field. We find the angular distributions of ionized electrons are affected by inclusion of the laser magnetic field for fields exceeding 100 a.u. with a result the appearance angles for the photoelectron deflected into the propagation direction.

## IONIZATION OF NEON AND KRYPTON IN A STRONG, ULTRAVIOLET, ULTRAFAST LASER FIELD

One of the recent areas in the study of strong fields has been the dependence of the rescattering on the drive laser wavelength. These investigations have focused on longer, mid-IR wavelengths where the promise of increasing the returning rescattering electron energy led to advances in the production of HHG. In addition to (e,2e) and HHG rescattering process, new results show the simultaneous excitation of as many as four or even six electrons on recollision via higher order (e,4e) and (e,6e) processes. These new higher order mechanisms extend traditionally accepted one or two electron interactions in strong field physics into a frontier whereby many of the electrons are excited in strong field processes. The proposed thermalization energy sharing between core electrons during recollision is a function of the timing, energy, and yield (or flux) of the excitation recollision electron. The time scale for this multielectron “thermalization” exchange has been reported to be 500 attoseconds, which is on the same time scale as the change in the laser electric field as one approaches ultraviolet wavelengths. The energy involved in recollision scales with the ponderomotive energy,  $U_p = E_0^2/4\omega^2$  in atomic units for a radiation field with a peak field of  $E_0$  and carrier frequency  $\omega$ . With higher intensities and longer wavelength lasers, rescattering energies have been extended beyond the keV range.

In this report we address the extension of rescattering processes to ultraviolet, 400nm wavelength laser pulses interacting with high ion charge states. The investigations presented here address issues related to wavelength dependence, such as the rescattering wave function spread in the continuum, and the matching of the rescattering energies to excitations in atomic and molecular systems. At short laser wavelengths there is less time for the ionized photoelectron wave function to spread in the continuum and the rescattering flux at the parent ion will correspondingly increase. The increased laser intensity required to ionize higher charge states also leads to greater rescattering energies. The involvement of higher intensities, multiple electrons and shorter recollision times make the work relevant

to potential new dynamics of attosecond recollision thermalization.

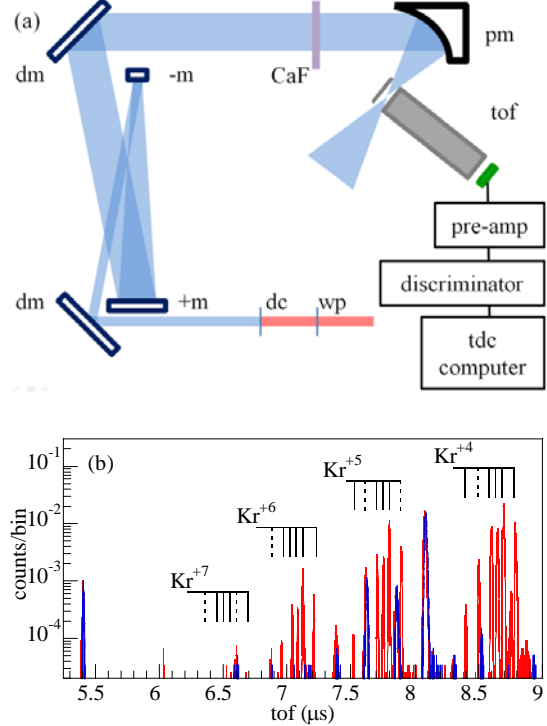


Fig. 1: Schematic of the apparatus (a) showing the  $\lambda/2$  waveplate (wp), doubling crystal (dc), dichroic mirrors (dm), negative (-m) and positive (+m) mirrors in the expansion telescope, 3mm thick vacuum CaF window (CaF), parabolic mirror (pm), and time-of-flight (tof) spectrometer with the associated signal electronics including the multi-hit time-to-digital converter (tdc). An example tof trace for Kr (red thin solid) and the background (blue solid) are shown in (b).

The experimental apparatus consisted of a kilohertz Ti:sapphire laser (3 mJ, 790 nm, 45 fs), terawatt Ti:sapphire laser (80 mJ, 40 fs, 790 nm), and high resolution time-of-flight ion spectrometer. The 790 nm fundamental radiation was doubled to 395 nm with a 0.2 mm thick BBO or 1 mm thick KDP. Once the laser beam was in the vacuum chamber, the high intensity was created by focusing the laser with an f/2 off-axis silver coated parabola. A skimmed, effusive atomic beam was crossed at 90° with the laser focus. The data is averaged into 15% intensity bins and each data point represents typically three independent collections of  $10^5$  shots. Ionization saturated in the collections at approximately  $10^6$  ions/shot-torr. The

laser intensity is estimated from optical and ion measurements to be within 50%. A schematic of the experiment is shown in Fig. 1(a) including the harmonic separation via two 400nm s-wave reflect, 800 nm p-wave transmit dichroic mirrors, a reflective 400 nm dichroic mirror expansion telescope, and 3 mm thick CaF vacuum window. A time-of-flight ion spectrum is shown in Fig. 1(b) collected with the background ( $< 2 \times 10^{-9}$  torr) and Kr sample gas ( $2 \times 10^{-7}$  torr). The major contaminants come from water and trace hydrocarbons, which at these intensities ionize to high charge states such as  $O^{4+}$ . The isotope structure in Kr ( $^{78}\text{Kr}$  0.4%,  $^{80}\text{Kr}$  2 %,  $^{82}\text{Kr}$  11.6 %,  $^{83}\text{Kr}$  11.5 %,  $^{84}\text{Kr}$  57 %,  $^{86}\text{Kr}$  17 %) can clearly be seen in the higher charge states, e.g.  $\text{Kr}^{6+}$  in Fig. 1(b). Peaks in  $m/q$  that are possibly contaminated by the background (dashed line in Fig. 1(b)) are either neglected in favor of signal from adjacent isotopes or only considered after careful background subtraction.

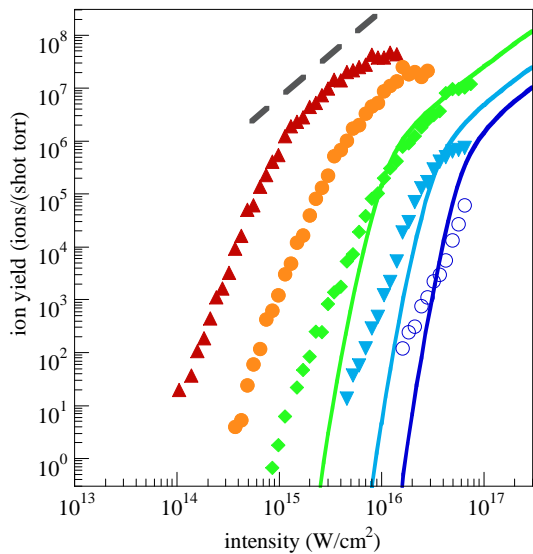


Fig. 2: Ionization yields of  $\text{Ne}^+$  (red),  $\text{Ne}^{+2}$  (orange),  $\text{Ne}^{+3}$  (light blue),  $\text{Ne}^{+4}$  (blue), and  $\text{Ne}^{+5}$  (black) as a function of intensity. An  $I^{3/2}$  (dash) ionization yield dependence is superimposed left of the saturated  $\text{Ne}^+$  yield.

The ionization yields of Ne and Kr at 400 nm from  $10^{13}$  W/cm<sup>2</sup> to  $10^{17}$  W/cm<sup>2</sup> are shown in Fig. 2 and Fig. 3. The data shown for the ionization of Ne is for charge states  $\text{Ne}^+$  to  $\text{Ne}^{+5}$ , which have ionization potentials of 21.6 eV and 126.2 eV, respectively. Small amounts of  $\text{Ne}^{+6}$  (158 eV) were observed near  $10^{17}$  W/cm<sup>2</sup> with event rates approximately one-tenth that of the  $\text{Ne}^{+5}$ .  $\text{Ne}^{+7}$  (207 eV) was not observed in

these studies. The experimental ion yields saturate near  $10^6$  ions/(shot-torr) above which the ionization yields scales at  $I^{3/2}$ . As a reference, the  $I^{3/2}$  intensity dependence is shown superimposed on  $\text{Ne}^+$  in the graph. For these ionization states at saturation the Keldysh parameter  $\gamma = \sqrt{I_p/2 U_p}$  (where  $I_p$  is the ionization potential energy) ranges from 1 for  $\text{Ne}^+$  near saturation to 0.1 for  $\text{Ne}^{+4}$  and  $\text{Ne}^{+5}$ . Based on the Keldysh parameter one expects a significant multiphoton component to the ionization of  $\text{Ne}^+$  and  $\text{Ne}^{+2}$  while the response of  $\text{Ne}^{+3}$ ,  $\text{Ne}^{+4}$ , and  $\text{Ne}^{+5}$  should be in the tunneling regime.

From above  $2 \times 10^4$  ions/(shot torr) to just below saturation the yields scale as approximately  $I^6$ . The break in slope from the  $I^6$  dependence at event rates near  $10^4$  ions/(shot torr) represents the involvement of two processes in the ionization generally identified as sequential, one-electron ionization (SI) of the ion and non-sequential ionization, multi-electron ionization (NSI) whose signature is a correlated ionization yield between multiple charge states. For the ionization yields  $\text{Ne}^{+3}$ ,  $\text{Ne}^{+4}$  and  $\text{Ne}^{+5}$  the two slopes are clearly observed and one can safely infer a non-sequential component in the ionization. NSI for these charge states at 800 nm diminishes as one proceeds from  $\text{Ne}^{+3}$  to  $\text{Ne}^{+5}$ , which is perhaps at first a counterintuitive result since at shorter wavelengths the rescattering energy available for excitation scales as  $\lambda^2$ .

The data for the ionization of Kr is shown in Fig. 3 for charge states  $\text{Kr}^{+1}$  to  $\text{Kr}^{+8}$  with ionization potentials from 14 eV to 126 eV, respectively.  $\text{Kr}^{+9}$  (231 eV) was not observed in these studies. As for the case of Ne, the experimental ion yields saturate near  $10^6$  ions/(shot-torr) above which the yields scale as  $I^{3/2}$ . For these ionization states at saturation  $\gamma$  decreases from 1.5 for  $\text{Kr}^+$  to 1.1, 1.0, 0.8, 0.7, 0.5, 0.4, and 0.3 as one proceeds up the ion charge states from  $\text{Kr}^{+2}$  to  $\text{Kr}^{+8}$ , respectively. The yields for Kr fall off more gradually than  $I^6$  as seen in neon. This is due in part to the lower ionization energies and multiphoton response at these intensities. The ionization of Kr is minimally a five photon process from the ground state at 400 nm. Based on the Keldysh parameter  $\text{Kr}^+$  and  $\text{Kr}^{+2}$  ionization is multiphoton and  $\text{Kr}^{+5}$ ,  $\text{Kr}^{+6}$ ,  $\text{Kr}^{+7}$ ,  $\text{Kr}^{+8}$  are in the

tunneling limit with  $\text{Kr}^{3+}$  and  $\text{Kr}^{4+}$  mixed in their ionization character. For all the ionization yields above  $\text{Kr}^{5+}$ , a non-sequential ionization component is observed from the measured break in slope for the intensity dependence of the yields near  $10^4$  ions/(shot torr).

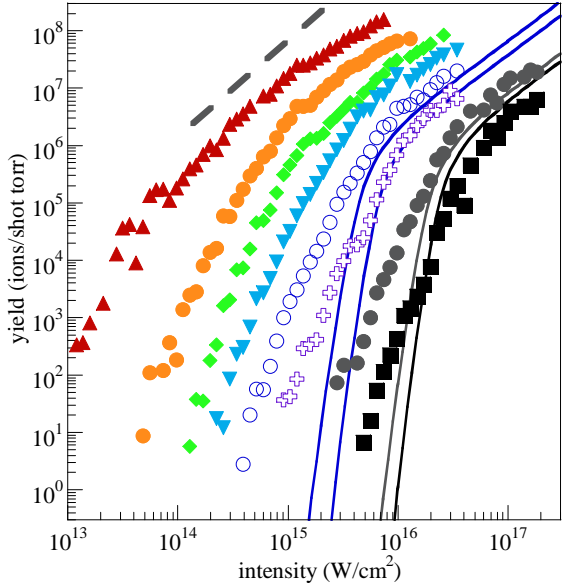


Fig. 3: (Color online) Ionization yields of  $\text{Kr}^+$  (red),  $\text{Kr}^{+2}$  (orange),  $\text{Kr}^{+3}$  (green),  $\text{Kr}^{+4}$  (light blue),  $\text{Kr}^{+5}$  (blue),  $\text{Kr}^{+6}$  (purple),  $\text{Kr}^{+7}$  (gray), and  $\text{Kr}^{+8}$  (black) as a function of intensity.

We use here a 1D, semi-classical, trajectory model of ionization. The results have been checked against a 3D semi-classical trajectory ensemble model described previously and found to be in good agreement. Similar models have been used to calculate the NSI ionization from rescattering in atoms and molecules. Briefly, it is a three step model comprised of (1) tunneling ionization followed by (2) continuum photoelectron dynamics and (3) rescattering interactions between the continuum photoelectron and the parent ion that incorporate inelastic (e,ne) scattering cross sections. The ionization is treated in the quasistatic limit where the frequency of the bound state electron is much greater than the laser frequency. Tunneling in this approximation is treated with the instantaneous electric field. In the calculation, the step size is  $7 \times 10^{-19}$  seconds and for each time step the rate is calculated using the field at that time. Following ionization, we use classical trajectories to simulate the tunneling photoionization current and continuum photoelectron.

The electron energy at the time of its ‘birth’, or appearance in the continuum, is set to be zero. The dynamics for the trajectories are calculated by solving the equations of motion with a Runge-Kutta ordinary differential equation solver. Starting with the neutral atom, the ionization is evaluated sequentially with respect to increasing charge. The determination whether the ionized electron revisits the parent ion is based on if the trajectory revisits the parent ion. When the electron revisits the parent ion the returning ensemble is converted to an electron rescattering flux. NSI due to rescattering is calculated using impact ionization; impact ionization cross sections when multiplied by the rescattering flux give our calculated (e, ne) rate. (e, 2e) and (e, 3e) cross sections were obtained from experiments and the Born-Bethe scaling law. For the sake of brevity in this summary the theory results will be highly abridged.

The calculated tunneling ionization yields for  $\text{Ne}^{3+}$ ,  $\text{Ne}^{4+}$ ,  $\text{Ne}^{5+}$ ,  $\text{Kr}^{5+}$ ,  $\text{Kr}^{6+}$ ,  $\text{Kr}^{7+}$ , and  $\text{Kr}^{8+}$  ions, where a tunneling description is expected to be accurate, are compared to the data in Figs. 2 and 3. The comparison shows tunneling accurately describe these ionization yields near saturation and help clarify the presence of NSI near  $10^4$  ions/(shot-torr) in Ne and Kr high charge states at 400 nm. Comparison of the tunneling yield to lower charge states (not shown in Figs. 2 and 3) is consistent with a multiphoton response as the tunneling yield accounts for only a few percent of the observed ionization.

While the NSI yield for  $\text{Ne}^{2+}$  and  $\text{Kr}^{2+}$  (Fig. 5) are very prominent at 800 nm, NSI at 400 nm for these charge states is strongly suppressed. On closer inspection of the rescattering energies available at saturation and the impact cross sections (Fig. 4), it is clear there is a balance between the two that can maximize NSI. Recent work into the wavelength dependence of rescattering began a process of characterizing the rescattering flux in a laser focus. It is possible to fit this energy dependent rescattering fluence,  $F_r(E)$ , with an empirical formula that is real for all energies  $E < E_{\text{cutoff}}$ ,

$$F_r(E) = \frac{A}{E_{\text{cutoff}}} \exp\left(\frac{6E}{E_{\text{cutoff}}}\right) \left(1 - \frac{E}{E_{\text{cutoff}}}\right)^2$$

where  $A$  is the scaling of the yield to the amount of ionization and in our calculations  $A$  also includes a

$1/\lambda^2$  dependence from the wave function spread in the continuum.  $E_{\text{cutoff}}$  is the maximum returning electron energy, typically  $3.2 U_p$ . Fig. 4 is a plot for the returning photoelectron energy spectra at  $51 \text{ TW/cm}^2$ ,  $64 \text{ TW/cm}^2$ ,  $80 \text{ TW/cm}^2$ , and  $100 \text{ TW/cm}^2$  for a laser pulse with a  $3.6 \mu\text{m}$  wavelength. This simple formula is surprisingly accurate in its two parameter fit to rescattering fluence.

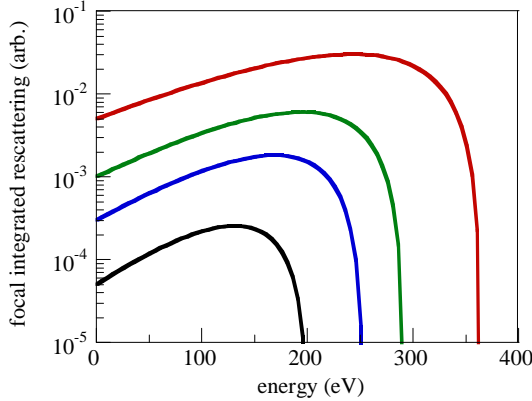


Fig. 4: Empirically calculated returning photoelectron energy spectra for  $100 \text{ TW/cm}^2$  (red),  $80 \text{ TW/cm}^2$  (green),  $64 \text{ TW/cm}^2$  (blue), and  $51 \text{ TW/cm}^2$  (black).

The ease with which the rescattering fluence can be calculated allowed a fuller investigation of the interplay between the rescattering fluence, impact cross sections, and laser wavelength. By multiplying the normalized rescattering fluence ( $\int_0^{E_{\text{cutoff}}} F_r(E) dE = 1$ ) with the (e,2e) cross sections ( $\int_0^{E_{\text{cutoff}}} F_r(E) \sigma(E) dE$ ) we obtain an estimate of where NSI will occur (Fig. 5). Each NSI yield is calculated at the saturation intensity of the given charge state since this is the intensity often used for the adjacent charge state NSI ratio and is the maximum in the NSI production for the interaction; for example, the NSI charge state ratio  $\text{Ne}^{2+}_{\text{NSI}}/\text{Ne}^+$  of 0.003 or  $\text{He}^{2+}_{\text{NSI}}/\text{He}^+$  of 0.002 measured at the saturation intensity for  $\text{Ne}^+$  and  $\text{He}^+$ , respectively. Using the saturation intensity sets the maximum rescattering energy for  $3.2 U_p$  and, since the ionization is essentially complete at that point, it is a common value for the amount of ionization and rescattering between charge states. The results are shown in Fig. 5(a) for the wavelength dependent NSI yields of  $\text{Ne}^{2+}$ ,  $\text{Ne}^{3+}$ ,  $\text{Ne}^{5+}$ , and  $\text{Ne}^{8+}$  and in Fig. 5(b) for  $\text{Kr}^{2+}$ ,  $\text{Kr}^{3+}$ ,  $\text{Kr}^{5+}$ , and  $\text{Kr}^{8+}$ . The units for the graph are adjusted to fit one experimental strong field

charge state ratio,  $\text{Ne}^{2+}/\text{Ne}^+$  of 0.003 at 800 nm. Beyond this, there is no adjustment made.

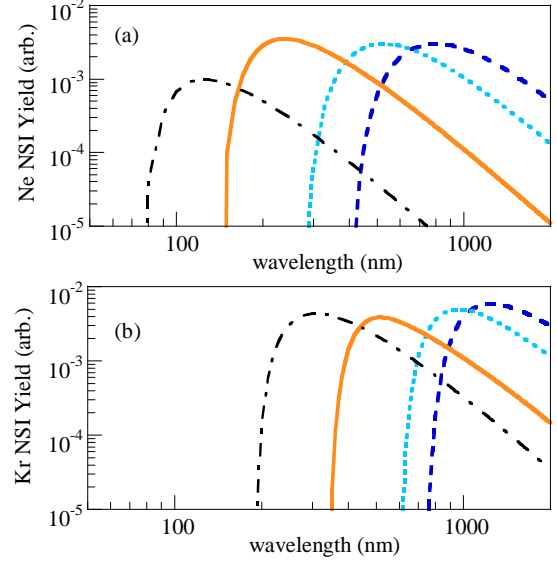


Fig. 5: Calculated NSI yields for Ne (a) as a function of wavelength for  $\text{Ne}^{2+}$  (blue dash),  $\text{Ne}^{3+}$  (light blue dotted),  $\text{Ne}^{5+}$  (orange solid), and  $\text{Ne}^{8+}$  (black dot-dash). Calculated NSI yields for Kr (b) as a function of wavelength for  $\text{Kr}^{2+}$  (blue dash),  $\text{Kr}^{3+}$  (light blue dotted),  $\text{Kr}^{5+}$  (orange solid), and  $\text{Kr}^{8+}$  (black dot-dash).

From an inspection of Fig. 5(a) one can see several properties of NSI as a function of wavelength. The NSI yield increases from a minimum cutoff wavelength where the rescattering energy from the ionization at saturation is less than the energy required to free the second electron in the (e, ne) collision, e.g. 80 nm for  $\text{Ne}^{8+}$  in Fig. 5(a). For wavelengths longer than this minimum, NSI increases to a peak value where the rescattering energy is matched to the maximum in the scattering cross section ( $10^{-3}$  at 120 nm for  $\text{Ne}^{8+}$ ). For even longer wavelengths, the NSI yield decreases as the peak in the rescattering fluence occurs at energies where the scattering cross section is decreasing and the rescattering fluence continues to decrease as  $1/\lambda^2$  due to the continuum wave function spread.

Despite the model's simplicity, it is able to capture many of the trends in current multielectron studies. At 800 nm the NSI yield is predicted to drop from a maximum for  $\text{Ne}^{2+}$  (0.003 in the figure representing the expected  $\text{Ne}^{2+}/\text{Ne}^+$  value) by an order of

magnitude for the NSI production of  $\text{Ne}^{5+}$  and another order of magnitude for the production of  $\text{Ne}^{8+}$ , an observation consistent with experimental measurements. In this study at 400 nm, Fig. 5(a) predicts the NSI from Ne will stay relatively constant from  $\text{Ne}^{3+}$  to  $\text{Ne}^{5+}$  as seen in Fig. 2. A similar finding in Kr occurs where the constant NSI observed in Fig. 3 for  $\text{Kr}^{5+}$  to  $\text{Kr}^{8+}$  is also seen in Fig. 5(b) where the predicted NSI is expected to be at the same yield level for  $\text{Kr}^{5+}$  and  $\text{Kr}^{8+}$  at 400 nm.

Prominent NSI is seen in the higher charge states when the atomic response to the external field is tunneling. A semiclassical model and simple scaling using an empirical formula for the rescattering fluence show that NSI not present in lower charge states at shorter wavelengths can appear and become prominent for higher charge states. The findings indicate that shorter wavelengths will give the highest NSI for higher charge states and the amount of NSI for a particular charge state can be optimized by picking the appropriate wavelength.

## PHOTOELECTRONS FROM ULTRASTRONG FIELDS

In the studies reported here, the electron final states for neon, argon, and xenon ionized by an ultrastrong field were experimentally resolved in energy ( $d\sigma/dE$ ) and polar angle ( $d^2\sigma/dEd\theta$ ). The ionization was created by an 800 nm, 40 fs pulse focused to a peak intensity of  $2 \times 10^{19}$  W/cm<sup>2</sup>. Adjustable slits selected the angle  $\theta$  admitted into a magnetic deflection spectrometer. The energy spectra (Fig. 1) reveal photoelectrons with energies from the highest measured yield at 50 keV up to a cutoff energy of 1.4 MeV for Ar and Xe, and 500 keV for Ne. The spectra for Ar and Xe both have modulations as a function of energy. The most prominent of these is the suppression in the Ar yield at 200 keV. Since the focus and laser is identical for Ne, Ar, and Xe, the cutoff energy and modulation in the spectra reflect atomic structure. An atom in the ultrastrong field may be thought of as continuously ionizing except between electron shells. The calculated ion populations for the atom as a function of time are shown in Fig. 2(a). As the laser pulse is increasing to its maximum intensity, deeper and deeper bound states are sequentially removed as the laser sweeps across the Coulomb field binding it. For

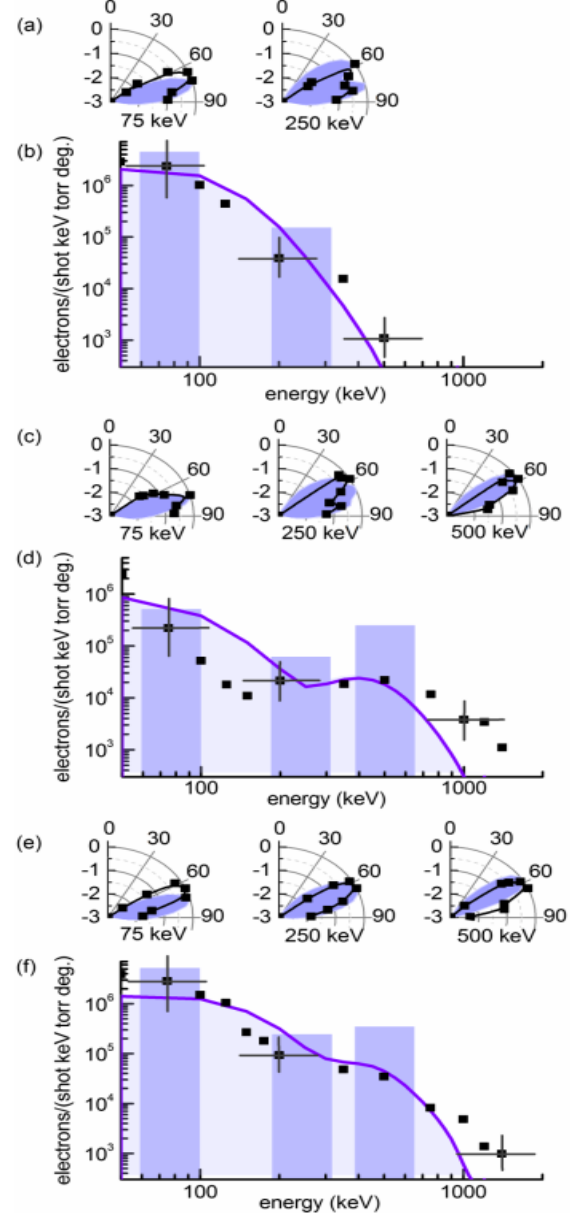


Fig. 1 Photoelectron energy spectra (PES) for  $\theta=72^\circ$  with angle, energy resolved photoelectron yields (AERPES) at 1.5 to  $2 \times 10^{19}$  W/cm<sup>2</sup>. (a) AERPES for neon at 75 keV and 250 keV. (b) PES for neon. (c) AERPES for argon at 75 keV, 250 keV, and 500 keV. (d) PES for argon. (e) AERPES for xenon at 75 keV, 250 keV, and 500 keV. (f) PES for xenon. In the AERPES polar plots the radial values are normalized and plotted on a  $\text{Log}_{10}$  scale from 0 to -3 (i.e. three orders of magnitude in the signal range). Measurements are shown with square symbols and a b-spline fit to aid the eye. The calculations are shown with a solid fill behind the data. The PES data is collected at  $\theta=72^\circ$  and shown with square symbols and representative error bars. Shaded rectangles indicate the regions where the AERPES collections are taken. The height of the bars (b,d,f) is the angle integrated yield (electrons/shot keV torr) at that energy. The calculations are shown with a solid line in (b,d,f) and fill in (a,c,e).

Ne, the  $n=2$  valence shell is removed well before the peak of the pulse. The final ion state is  $\text{Ne}^{8+}$  since  $10^{19} \text{ W/cm}^2$  is insufficient to ionize the 1s electron (IP = 1362 eV). For Ar, early in the pulse the  $n=3$  shell (Ar to  $\text{Ar}^{8+}$ ) ionizes and then nearer to the peak of the pulse the  $n=2$  shell ( $\text{Ar}^{9+}$  to  $\text{Ar}^{16+}$ ). Xe ionization begins with the 5p electron (IP = 12 eV) and proceeds through the pulse until reaching  $\text{Xe}^{26+}$ . Contrasting with traditional strong fields, where photoionization is viewed as a ‘stepwise’ process involving one- or two-electrons ionizing during the pulse and appearing distinctly in the continuum, ultrastrong fields involve many charge states and photoionization becomes essentially continuous for electrons removed from an atomic shell. Between shells, such as the  $n=2, 3$  in Ar, ionization shuts off as can be seen in the stagnant  $\text{Ar}^{8+}$  yield 40 fs before the peak of the pulse (Fig. 4(a)). Consequently, there is a reduction in electrons with energies produced at that field strength. For argon, this is manifested as the dip in the yield at 200 keV (Fig. 3(d)). For neon, ionization shuts off after the  $n=2$  shell, explaining the simple structure in the measured and calculated yield (Fig. 3(b)) and lack of photoelectrons at the highest, MeV energies. For Xe, the modulation in the ionization yield is less striking since there is a lack of distinction between the  $n=4$  and  $n=5$  electron shells (due to the energy shift of the 4d electrons) and ionization is only briefly interrupted ( $\text{Xe}^{8+}, \text{Xe}^{18+}$ ) during the rise in the laser pulse.

In the continuum, the photoelectron kinetic energy approaches and exceeds the rest mass (Fig. 1). As the electron velocity is driven by  $E_{\text{laser}}$ , the photoelectron is deflected by the

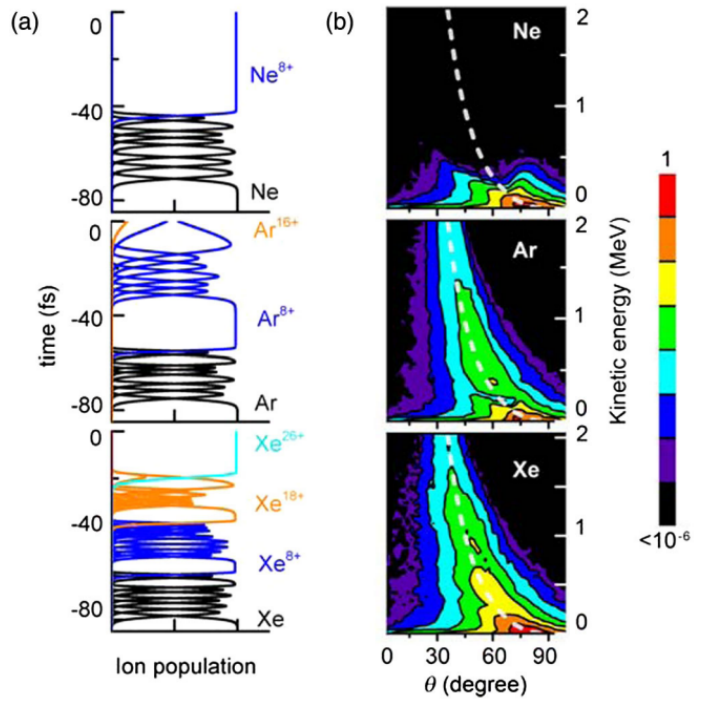


Fig. 2 Calculated ion populations and energy, angle resolved photoelectron yield for neon, argon, and xenon for a laser pulse with a peak intensity of  $2 \times 10^{19} \text{ W/cm}^2$ . a, Time resolved ion populations for neon, argon, and xenon as a function of time from before (-85 fs) to the peak of the laser pulse (0 fs). b, Energy, angle resolved photoelectron yield for neon, argon, and xenon. The yield is integrated from the peak intensity ( $2 \times 10^{19} \text{ W/cm}^2$ ) to regions in space and time where the intensity is  $2 \times 10^{17} \text{ W/cm}^2$ . Slices from the energy, angle resolved photoelectron yield at 75 keV, 250 keV, and 500 keV, convoluted with the experimental energy and angle resolution are shown in the polar plot comparisons with the experiment in Fig. 3(a,c,e). The dashed line superimposed on the plots represents the relationship expected with plane wave light. The eight level color scale in (b) ranges from red (1) to black ( $< 10^{-6}$ ).

Lorentz force into the laser propagation direction since  $E_{\text{laser}} \times B_{\text{laser}}$  is along  $k_{\text{laser}}$ . The

effect of the Lorentz force can be seen in the polar angle, energy resolved yields (Fig. 1(a,c,e)). The measured values (mean  $\pm$  standard deviation) at 75 keV are  $75^\circ \pm 6^\circ$ ,  $79^\circ \pm 7^\circ$ , and  $72^\circ \pm 6^\circ$  for Ne, Ar, and Xe, respectively, and at 500 keV are  $63^\circ \pm 7^\circ$  and  $67^\circ \pm 7^\circ$  for Ar and Xe, respectively. The simple relationship between the electron energy and forward deflected angle in a plane wave is significantly modified by the curvature of the laser focus wave front. In our experiments the  $\exp(-2)$  irradiance contour asymptote of the laser focus approaches a cone angle of  $\theta = \frac{\lambda}{\pi w_0} = 11^\circ$ , where  $w_0$  is the  $\exp(-2)$  irradiance radius at the focus. The final state photoelectron emission angle is a result of  $E_{\text{laser}}$  and  $B_{\text{laser}}$  forces after ionization as the electron gains energy from the field. The agreement with the calculated angular distributions (also shown in Fig. 1(a,c,e)) indicates the  $6^\circ$  to  $7^\circ$  width in the emission angle is a result of the angular range of  $k_{\text{laser}}$  across the outgoing wave front and the mean polar angle is primarily a function of the emitted photoelectron energy (the mean emission angle for neon, argon, and xenon at 75 keV, for example, are all the same within the  $\pm 4^\circ$  measurement accuracy). A comparison between the calculated energy, angle resolved yield with a plane wave and the experimental focus is shown in Fig. 2(b). Broader polar angular distributions (for example in Ar at 250 keV) occur when the emission at that angle is suppressed and contributions to the yield are coming from ionization prior to or after the intensity that would normally create electrons at that energy.

Atomic ionization in ultrastrong fields gains new dynamics from the role of the  $B_{\text{laser}}$ , relativistic motion, extended laser focus, and a change in the role of atomic structure from individual electrons towards the electron shell structure. The observed strongly forward scattered photoionization is in agreement with classical field scattering employing the full nonparaxial  $E_{\text{laser}}$ ,  $B_{\text{laser}}$  field. The detailed experiments supported by theoretical results show relativistic effects are limited to the continuum and ionization at ultrastrong intensities of order  $10^{19}$  W/cm $^2$ , bound states of order  $10^2$  to  $10^3$  eV may still be treated in the dipole limit.

## RECONSTRUCTING LONGITUDINAL STRAIN PULSES USING TIME-RESOLVED X-RAY DIFFRACTION:

Laser induced carrier dynamics in a gold film were characterized by a time-resolved x-ray diffraction (TRXRD) experiment. In particular we monitored the temporal evolution of the Au (111) diffraction peak from the 270 nm gold film (see figure 1). Upon ultrafast excitation, a shift in the diffraction peak to lower angles ( $\theta - \theta_b$ ) is observed. Fitting the x-ray diffraction peaks to a series of Gaussian curves, we quantified the temporal dynamics in the peak shift, which indicates that the gold lattice has expanded by  $\sim 0.1\%$  in under 10ps, consistent with previously published results. Using the accepted value of the lattice expansion coefficient of bulk gold ( $1.4 \times 10^{-5} K^{-1}$ ), the resulting lattice expansion indicates that the gold film has increased in temperature by  $\sim 100K$ . At intermediate time delays ( $10\text{ps} < \Delta T < 100\text{ps}$ ), the location of the gold diffraction peak changes minimally,

and by 650ps, the peak has returned to its pre-pumped position indicating the cooling process takes on order of 500ps. Following the gold film experiments, we proceeded to measure the TRXRD patterns of the photoexcited gold coated Ge (111) crystals. In Figure 1, differential diffraction intensity of X-ray Bragg diffraction patterns from Ge (111) substrates are shown. The x-ray diffraction intensity is normalized by the intensity of the Cu- $K_{\alpha 1}$  diffraction peak. For comparison, we also include the differential diffraction intensity of an uncoated Ge (111) crystal (figure 1). Upon inspection, there are several distinct differences between the coated and uncoated samples. The uncoated sample demonstrates an almost universal increase in diffraction efficiency for all angles (indicating the generation of additional sideband components at times longer than 20 ps) as well as a global peak shift to lower diffraction angles (indicative of ‘static’ surface heating). For both the 50nm and 100 nm gold film coated Ge crystals, positive diffraction sidebands are

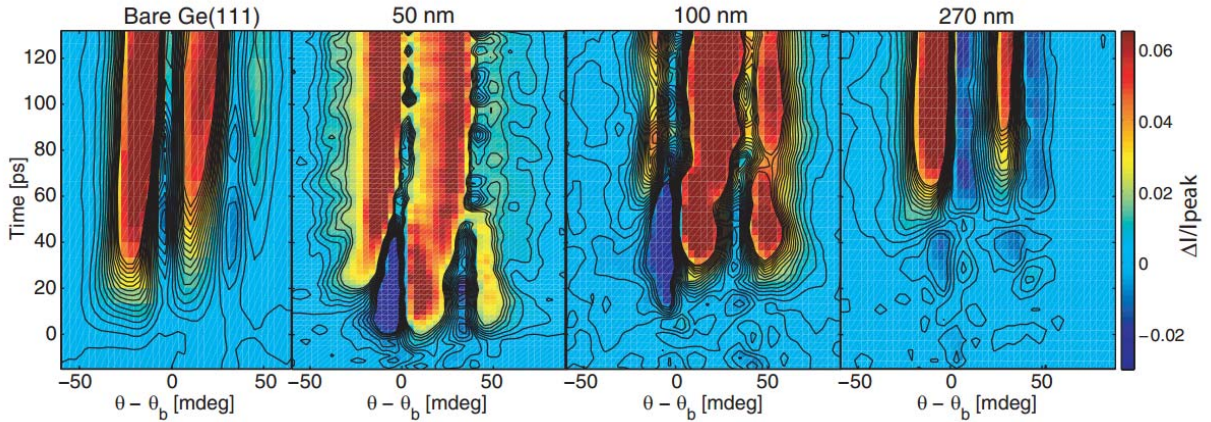


FIG. 1. Differential TRXRD measurements of gold-coated Ge(111) crystals of various thicknesses. Left to right: uncoated Ge and 50-nm, 100-nm, and 270-nm gold films.  $\theta_b$  represents the Bragg angle for the undisturbed Ge(111) peak on Cu  $K_{\alpha 1}$  radiation.

observed immediately after laser excitation, where the maximum angular shifts appear at 30 ps and 53 ps respectively. Following the positive sidebands, the maximum negative angular shift from 50 nm gold film,  $\sim 50$  mdeg, is observed at  $\sim 66$  ps while negative sidebands up to 25 mdeg are apparent at 83 ps for the 100 nm film. The temporal shift between the generation of positive and negative sidebands demonstrates that the strain in the Ge substrate is a bipolar acoustic pulse. In addition, the different maximum angular shifts of two samples, is consistent with the generation of the maximum wavevector generation being determined by the thickness of the metallic film.

In figure 2, we show the retrieved spectral amplitude and phase for each of the diffraction angles measured in the TRXRD pattern shown in figure 1. The Fourier transform makes it clear that the angular shift of sideband is proportional to the oscillating frequency, consistent with the acoustic dispersion relationship. Meanwhile, there is an obvious  $\pi$  phase shift between the negative and positive sidebands. Looking at the retrieved spectral amplitude from the Fourier transform, there is a clear asymmetry to the spectra of the positive and negative wave vectors. This asymmetry is likely due to a slight ‘static’ temperature rise of the Ge substrate ( $< 10$ K), which shifts the whole rocking curve to smaller diffraction angles and increasing the observed amplitude of the oscillations.

The ultimate retrieval of the spatio-temporal strain profile is limited by the angular

resolution of our setup. In figure 2b we numerically reconstruct the strain profile by performing a Fourier sum of the amplitude and phase retrieved from the negative sidebands for the 50nm gold coated sample. With our experimentally limited number of modes, we see a series of strain pulses at a characteristic period associated with the angular resolution of our experiment. Even with this limitation, we can retrieve some insight into the spatio-temporal profile of the acoustic pulse. For example, we observe that the pulse is bipolar with a very rapid change in sign ( $< 50$ nm) consistent with the observed coherent sideband generation. However, what is somewhat surprising in

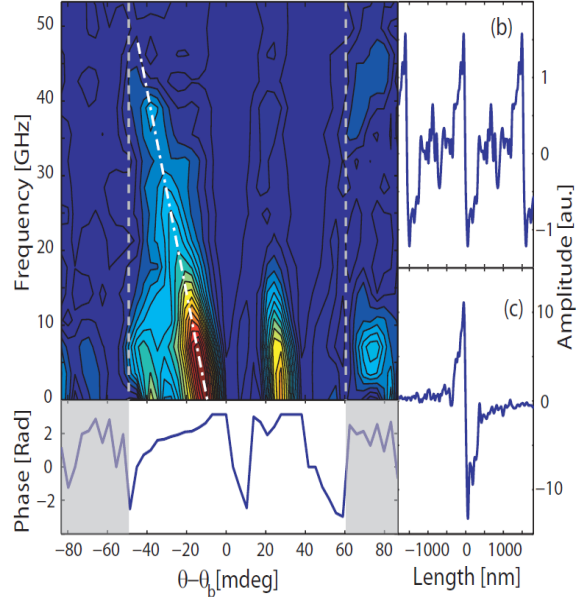


FIG. 2 Spectral amplitude and phase of sidebands retrieved from the TRXRD patterns observed from 50 nm thick films. Dashed line is a guide to the eye. (b) The reconstructed spatial profile of the acoustic pulse using the data as shown. (c) The reconstructed spatial profile of the acoustic pulse obtained by adding 9 interpolated points for each data point.

the Fourier reconstruction, is the spatial extent of the acoustic pulse. It has been widely assumed that the spatial extent of the generated acoustic pulse will have a scale that is approximately twice the thickness of the metallic film. However, we find that the acoustic pulse has a spatial extent greater than 500nm, an order of magnitude larger than the gold film thickness. In particular, we perform a simple nine point interpolation on the data prior to Fourier reconstruction. After reconstruction, we now find that the data reveals an isolated bipolar acoustic pulse, with a sign change of less than 50nm and a spatial extent of over  $>500\text{nm}$ . The observation of this spatio-temporal elongation has not been reported in prior time domain optical or TRXRD studies. These studies show it is possible to use x-rays from ultrafast laser matter interactions to perform time resolved x-ray diffraction and then unambiguously invert the diffraction signal to find changes in the separation between atoms, i.e. the strain dynamics.